Distribution of trace and rare earth elements in the estuary of Ría de Huelva (SW Spain): Field data and geochemical modeling

Joan Gutiérrez-León, Ricardo Millán-Becerro, Sergio Carrero, Rafael Pérez-López, Elina Ceballos, Rémi Freydier, Josep Soler, Jordi Cama

Chemical Geology 662 (2024) 122208

Contents lists available at ScienceDirect

Chemical Geology

journal homepage: www.elsevier.com/locate/chemgeo

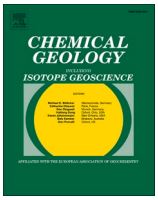

Distribution of trace and rare earth elements in the estuary of Ría de Huelva (SW Spain): Field data and geochemical modeling

Joan Gutiérrez-León [a,*], Ricardo Millán-Becerro [b], Sergio Carrero [a], Rafael Pérez-López [b], Elina Ceballos [a], Rémi Freydier [c], Josep M. Soler [a], Jordi Cama [a,*]

[a] Institute of Environmental Assessment and Water Research (IDAEA), CSIC, 08034 Barcelona, Catalonia, Spain
[b] Department of Earth Sciences & Research Center on Natural Resources, Health and the Environment (RENSMA), University of Huelva, Campus 'El Carmen', 21071 Huelva, Spain
[c] HydroSciences Montpellier, Université de Montpellier, CNRS, IRD, Montpellier, France

ARTICLE INFO

Editor: Karen Johannesson

Keywords:
Rare earth element (REE)
Metals
Adsorption modeling
Geochemical distribution
Estuary

ABSTRACT

The geochemistry of the Ría de Huelva estuary (Spain) has been widely studied owing to its unique conditions due to mixing of acid mine drainage (AMD), river water and seawater, which have been aggravated by the existence of an adjacent phosphate fertilizer plant and its associated phosphogypsum stack.

To better understand the complex geochemistry of the overall estuarine system, we make use of (1) measured concentrations of relevant trace elements (rare earth elements (REEs) and metal(loid)s) in the sediments and waters of the estuary and (2) geochemical modeling which combines mixing and adsorption processes.

Our study sheds light on the elemental distribution in the sediments and water in the water-mixing area. As seawater neutralizes the acidity of the river water (pH increases to 6.2) colloids of Fe- and Al-oxyhydroxysulphates (schwertmannite and basaluminite, respectively) precipitate as concentrations of aqueous Fe and Al increase. These phases have a high adsorption capacity and play a critical role in the geochemistry of the aquatic system by retaining Cu, Pb, Cr, As, P, REEs and smaller amounts of Zn, Co, Ni and Mn. The geochemical model reproduces the behaviour of the aqueous REEs, requiring high S/L ratios at pH $\geq$ 3.5 and participation of sediments and colloids in the reactions to match the field data.

The evaluation of the effect of the adjacent phosphogypsum stack on the estuarine geochemistry shows that the stack has a notorious impact on the geochemistry of the surrounding estuarine environment owing to the release of high quantities of phosphate.

1. Introduction

Acid Mine Drainage (AMD) is characterized by high acidity and large concentrations of sulphate, metals, and metalloids. AMD in the Iberian Pyrite Belt (IPB) mainly results from the oxidative dissolution of pyrite, which is associated with a few active mines and about one hundred abandoned Fe-sulphide mines (Grande et al., 2010; Nieto et al., 2013; León et al., 2021; Cánovas et al., 2022).

AMD in the IPB region shows high concentrations of rare earth elements (REEs) (between hundreds and thousands of μg L^{-1} (Galán et al., 2003; Sánchez España et al., 2005; Ferreira da Silva et al., 2009; Ayora et al., 2013, 2016; Grande et al., 2018; Cánovas et al., 2020, León et al., 2023)). Given the importance of these elements for the development of new technologies (Chakhmouradian and Wall, 2012; Gwenzi et al., 2018), AMD in the IPB has been proposed as a potential secondary source of REEs (León et al., 2023).

The extensive IPB-AMD pollutes the Tinto and the Odiel rivers, which eventually discharge at the estuary of Ría de Huelva (Sánchez España et al., 2005; Nieto et al., 2013) (Fig. 1). Major and trace elements dissolved in this estuarine system (e.g., Fe, Al, S, Zn, Cu and As, Cd, Co, Ni, Mn and Pb, respectively) have been studied by several authors (Grande et al., 2000, 2003; Olías et al., 2006; Cánovas et al., 2007, 2012; Lecomte et al., 2017). Cánovas et al. (2012) quantified the dissolved pollutant load of the Odiel river over the course of 8 days, resulting in a total of 226 t of sulphate, 13 t of Al, 5.3 t of Zn, 3.2 t of Mn, ~1.9 t of Cu, 1.7 t of Fe, and lesser amounts of other metals (92 kg of Co, 47 kg of Ni, 24 kg of Pb, 17 kg of Cd, etc.). Since the AMD-polluted waters mix with seawater in the estuary, most of the metals lose their mobility as a result

* Corresponding authors.
E-mail addresses: jgleon18@gmail.com (J. Gutiérrez-León), jordi.cama@idaea.csic.es (J. Cama).

https://doi.org/10.1016/j.chemgeo.2024.122208
Received 28 March 2024; Received in revised form 29 May 2024; Accepted 5 June 2024
Available online 6 June 2024

of the increase in pH, yielding losses between the riverine and seawater concentrations of 76% Cu, 64% Zn, 45% Co, 14% Cd and 12% Ni (Braungardt et al., 2003). Moreover, the interaction between the polluted waters and the estuarine sediments influences the mobility of contaminants. Precipitated basaluminite and schwertmannite can retain some of the pollutants (e.g., As, REEs and Cu) via sorption whereas Zn, Cd, Ni, Co and S behave conservatively (Pérez-López et al., 2023). Despite having losses of these elements, the AMD-impacted system still produces an extensive plume of contamination with regard to Mn, Cu, Cd and Zn, extending south towards the Strait of Gibraltar (Elbaz-Poulichet et al., 2001).

As for the mobility and distribution of rare earth elements (REEs) in the IPB-AMD region, recent studies observed that in areas where the AMD polluted rivers mixed with pristine streams, the acidity was neutralized and REE-retaining Fe- and Al- oxyhydroxysulphates were formed (Lozano et al., 2019a, 2020a). However, the pH of the mixing conditions did not allow schwertmannite ($Fe_8O_8(OH)_6SO_4{\cdot}nH_2O$) to be a relevant sink for these elements whereas basaluminite ($Al_4SO_4(OH)_{10}{\cdot}5H_2O$) was capable of scavenging some of these elements (Lozano et al., 2020b).

The REE distribution has been also tested in dispersed alkaline substrate (DAS) passive remediation plants (Caraballo et al., 2009a, b, 2011a, b; Macías et al., 2012), where AMD is neutralized using chemical reagents, such as calcite and MgO, to increase the pH at conditions where the REEs can be recovered from newly-formed precipitates (Ayora et al., 2013). However, since few AMD-impacted streams are remediated with passive systems and most of the newly-formed precipitates at confluences are unable to retain the REEs, these elements remain dissolved in AMD (Lozano et al., 2020a). Under these circumstances, most of the REEs and other contaminants are transported to the estuary of Ría de Huelva, where acidity of AMDs is neutralized by seawater mixing and the aqueous concentration of REEs decreases (Elbaz-Poulichet and Dupuy, 1999).

Little research has focused on REE mobility in the Ría de Huelva estuary. Borrego et al. (2005) studied the distribution of REEs in three sediment cores of the Huelva estuary retrieved at pH between 2.5 and 5. These authors found that the estuarine sediments were depleted in REEs under acidic conditions and their concentrations increased as the pH rose. Moreover, as regards the North American Shale Composite (NASC) ratios, the authors showed a depletion of light REEs (LREE) with respect to middle REEs (MREE) and heavy REEs (HREE). Borrego et al. (2012) found that the high concentration of REEs in fluvial waters (Σ[REE] = 1090 μg L^{-1}) dropped about one order of magnitude (Σ[REE] ≤ 199 μg L^{-1}) after the AMD river mixed with seawater, providing evidence that dilution and precipitation reactions led to REE depletion. However, the interaction between the solids and the supernatant solutions remains unknown. Experimental approaches in REE behaviour during seawater and AMD mixing have shown that an increase in pH induced the precipitation of poorly and highly organized Fe-bearing phases (e.g. jarosite, goethite and schwertmannite), which concentrated REE in their structure (Lecomte et al., 2017). These approaches considered two end-member solutions (one taken from pure AMD and another from the seawater), and by varying their respective volumes they tried to reproduce the mixing processes in the estuary. However, no effect of phosphogypsum wastes was considered in these studies, which is an important factor that might affect the geochemical system of the estuary. Phosphogypsum is an undesired by-product mainly composed of gypsum ($CaSO_4{\cdot}2H_2O$), impurities (e.g., As and Cd) and radionuclides (e.g., U, Ra and Rn) from the production of phosphate fertilizers (Macías et al., 2017; Rutherford et al., 1994). In the estuary, around 100 Mtons of this waste are stored in a stack (Figs. 1 and 2). Some studies point out that the intertidal estuarine water accesses the phosphogypsum stack, washing the waste at depth and returning to the estuary in the form of edge outflows (Papaslioti et al., 2018; Pérez-López et al., 2016; Millán-Becerro et al., 2023).

Considering the earlier studies of REE mobility in the estuarine system, the REE transference from solution to a colloidal phase and the role of potential polluting elements (e.g. heavy metals), our study seeks

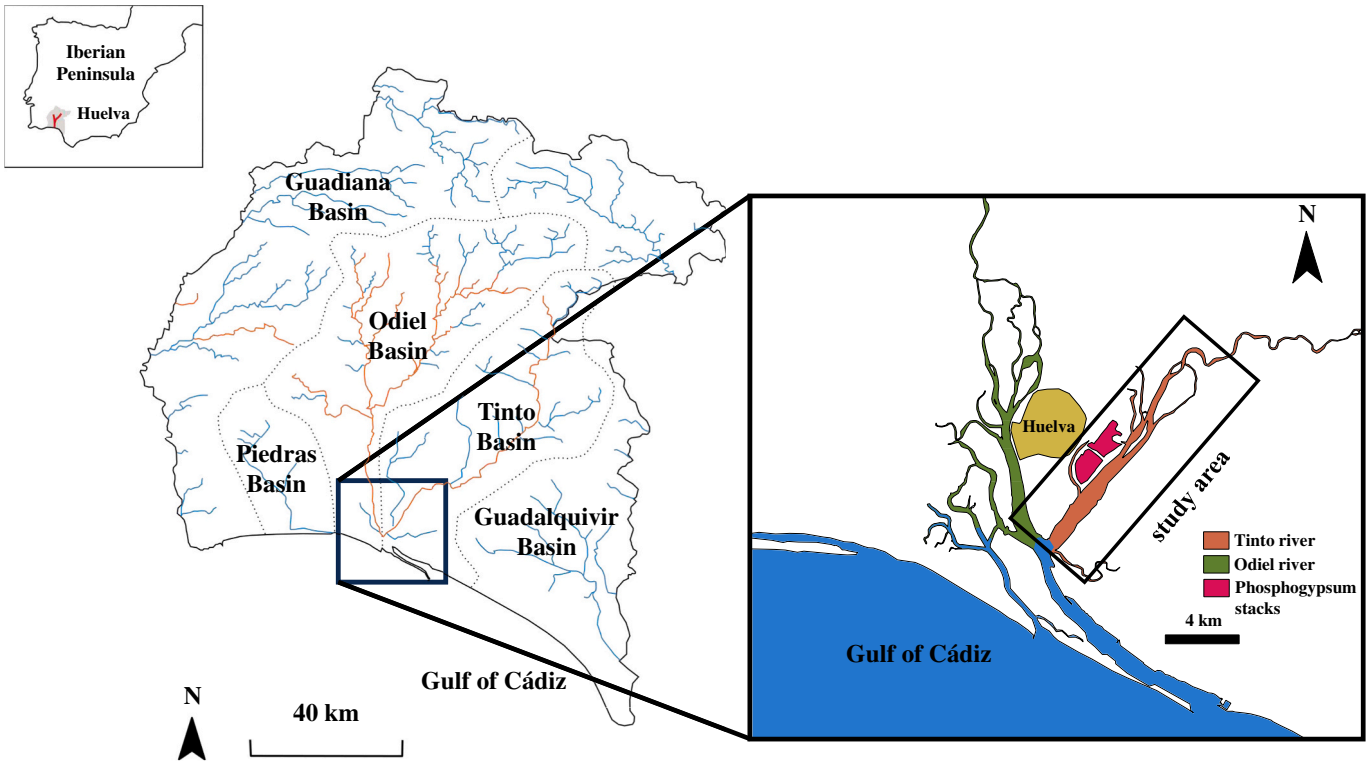

Fig. 1. The study area (estuary of Ría de Huelva) is located in the south of the Iberian Peninsula. The confluence of the Tinto and the Odiel rivers occurs in the estuary. The phosphogypsum stack alongside the Tinto river is shown.

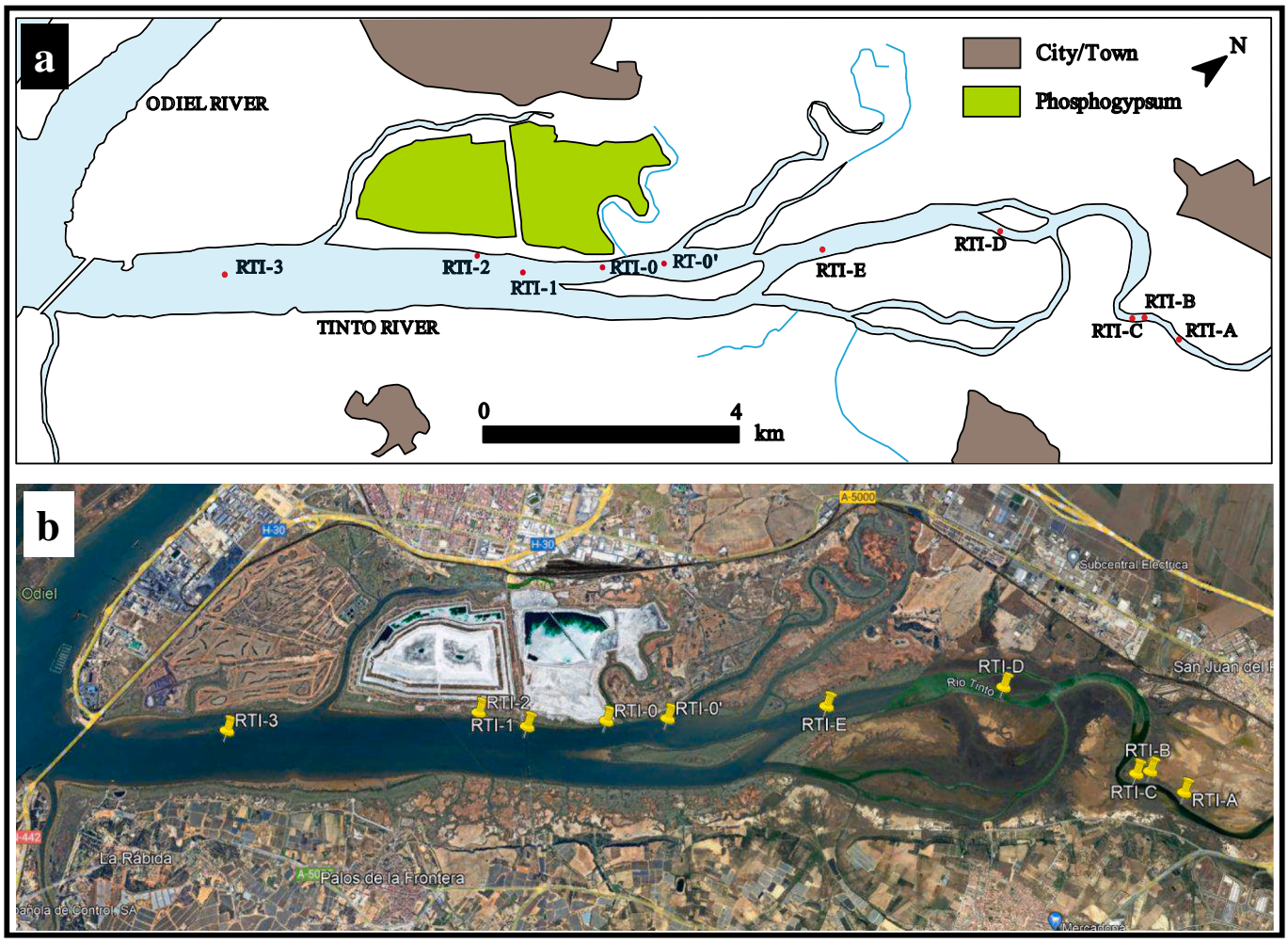

Fig. 2. Estuary of Ría de Huelva (the Tinto river sub-estuary): a) schematic map and (b) Google Earth image indicating sampling points and phosphogypsum stack.

to determine the processes involved in the partitioning and distribution of heavy metals and REEs as the AMD neutralization by seawater mixing occurs. To this end, solid samples from shallow surface sediments, aqueous samples containing colloidal matter, and supernatant water from the top of cores were collected along the estuary mixing area. Moreover, REE adsorption models, using novel thermodynamic data related to REE adsorption onto schwertmannite and basaluminite, were developed to shed light into the mechanisms governing the REE geochemistry of the Ría de Huelva estuary.

2. Materials and methods

2.1. Study area

The Odiel and the Tinto rivers (Fig. 1) have a length of 140 km and 100 km, respectively, and the estimated annual flows are 500 hm^3 $year^{-1}$ and 100 hm^3 $year^{-1}$, respectively (Sánchez España et al., 2005; Nieto et al., 2013). Many AMD streams from abandoned sulphide mines are tributaries along both rivers (Sánchez España et al., 2005). The confluence of both rivers occurs in the estuary (Fig. 1). For forty years, phosphogypsum material has been dumped over a huge stack (Fig. 1) that is adjacent to the Tinto river (Millán-Becerro et al., 2023). The Mediterranean climate of this area is characterized by long periods of drought and intense rainy events. Approximately 70% of the annual rainfall occurs between October and February, with the mean annual rainfall being 600 mm (Cánovas et al., 2016). The highest concentration of dissolved metals is in autumn and early winter during rain events when dissolution of evaporitic salts, which precipitated in summer, takes place (Cánovas et al., 2012).

2.2. Solid and liquid sampling

In a two-day sampling campaign (January 2023), two types of samples were collected along the Tinto River sub-estuary mixing area (sampling points shown in Fig. 2). The first type of samples consisted of cores of shallow surface sediments that were extracted at all sampling points at depths of 10–50 cm except at RT-A. A rod-operated sampler with a closable cutting head was used (Fig. 3), enabling us to collect solid material and supernatant water. The second type of samples were shallow water suspensions collected at RTI-0 and RTI-1 sampling points at a depth of ≈ 2 m (Fig. 2) containing suspended particulate matter (size <62 μm), which included colloids (size of 0.1-1 μm). Water temperature, pH, ORP and EC were measured at the sampling points (Table S1).

From the shallow water samples collected at RTI-0 and RTI-1 sampling points, suspended particulate matter and a colloidal fraction (particles between 0.45 μm and 1 μm) were obtained by filtering 23 L (RTI-0) and 16 L (RTI-1) of water suspension through 0.45 μm membranes. Clean filters were dried at 35 °C for 24 h and weighted. After particle saturation, the filters were freeze-dried and weighted. Amounts of 0.628 g and 2.087 g were retrieved from RTI-0 and RTI-1, respectively. Some shallow water suspension and supernatant waters were filtered through 0.22 μm nylon membranes and were acidified with 1% of HNO_3 solution (65% HNO_3; Merck) for inductively coupled plasma

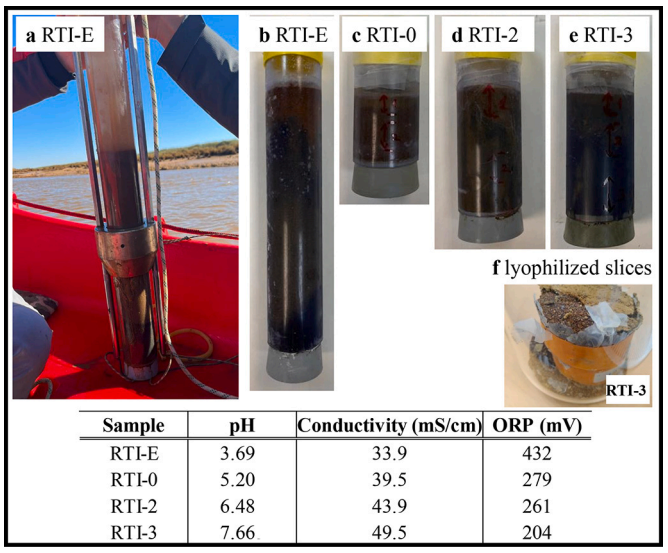

Sample	pH	Conductivity (mS/cm)	ORP (mV)
RTI-E	3.69	33.9	432
RTI-0	5.20	39.5	279
RTI-2	6.48	43.9	261
RTI-3	7.66	49.5	204

Fig. 3. Photographs of an extracted core (in-situ supernatant and sediment) at sampling point RTI-E (a) and sediment cores at RTI-E (b), RTI-0 (c), RTI-2 (d) and RTI-3 (e) (see Fig. 2) and two lyophilized slices from the RTI-3 core (f). The RTI-E sediment core is 50 cm long, and the diameter of the cores is 8 cm. pH, conductivity and ORP of the in-situ supernatant water extracted from each core are displayed.

mass spectroscopy (ICP-MS) analysis.

From the cores of shallow surface sediments, pH, EC and ORP of the supernatant water of the top core samples were measured. The solid material of the cores was frozen and sliced to obtain several layers of 1–5 cm in thickness from top to bottom, which were lyophilized (Fig. 3). Sediments and colloids were analyzed with powder X-Ray diffraction (XRD) using a 2θ goniometer Bruker D8 Advance diffractometer to identify crystalline Fe-bearing minerals. Small amounts (≈ 2 g) of the collected sediments were ground to a size of 60–200 μm using agate mortar and pestle.

2.3. Sequential extraction

A modified procedure of the sequential extraction proposed by Dold (2003) was performed with the colloidal and sediment samples (Caraballo et al., 2009b; Lecomte et al., 2017). The sequential extraction consisted of a 6-step selective dissolution that involved 1) the water-soluble phase, 2) the carbonate and exchangeable phases, 3) the poorly ordered metal oxyhydroxides, oxyhydroxysulphates and Mn-hydroxides, 4) the highly ordered metal oxyhydroxides, 5) the organic matter and 6) the residual phase.

Half a gram (0.5 g) of each sample was used for the overall procedure. After each step, the sample and the corresponding solution were centrifuged for 15 min at 4500 rpm. The supernatant and solid samples were then separated, and the liquid was filtered through 0.22 μm nylon membranes and acidified with 1% of HNO_3 (65% HNO_3 Merck) solution. In each step, a blank sample was subjected to the same procedure and analyzed accordingly.

Step 1 consisted of stirring the sample in 50 mL of Milli-Q water for 1 h; in step 2, a total of 20 mL of 1 M ammonium acetate was added to residue of the first step and the solution was shaken for 2 h; in step 3, 20 mL of 0.2 M ammonium oxalate that was acidified to pH with 0.2 M oxalic acid solution were added to the residue of step 2 and shaken for 1 h in total darkness; in step 4, 20 mL of a 0.2 M ammonium oxalate solution were mixed with the residue of step 3 and shaken at 80 °C for 2 h in a water bath; in step 5, the residue of step 4 was mixed with 10 mL of 30% *w/v* (8 M) H_2O_2, allowing evaporation until the volume reduced to 3 mL. Subsequently, another 10 mL of 8.8 M H_2O_2 were added and heated at 85 °C for 1 h to reduce the volume to 3 mL. After this, 10 mL of 1 M ammonium acetate solution acidified with acetic acid to pH 4.5 were added and shaken for 16 h at room temperature; the final step consisted of a regular digestion using 7.5 mL of HF (40%: Merck), 2.5 mL of $HClO_4$ (60%; Merck) and 2.5 mL of HNO_3 (65%; Merck) for the residual matter.

A bulk extraction of all materials (using 0.250 g) was performed to calculate a REE recovery percentage [%Recovery = (step1 + step2 + step3 + step4 + step5 + step6)/bulk extraction] according to the procedure by Quispe et al. (2012) and Lecomte et al. (2017). The recovery percentage of the REEs was between 85 ± 19% (La) and 112 ± 19% (Tm) with a mean of 99.8%.

2.4. Analytical techniques

pH from collected estuary suspensions was measured with an accuracy of 0.02 pH units at room temperature with a Crison® glass electrode calibrated with buffer solutions at pH 2, 4, 7 and 9. ORP and pH were measured using a multi-parameter 3510 device (WTW). Conductivity was measured using the WTW conductivity portable meter Profiline Cond 3110 Set 1. Concentrations of the trace elements (Li, B, V, Cr, Mn, Co, Ni, Cu, Zn, As, Rb, Sr, Y, Mo, Cd, Sn, Sb, Ba, La, Ce, Pr, Nd, Sm, Eu, Gd, Tb, Dy, Ho, Er, Tm, Yb, Lu, Tl, Pb and U) in the sequential extraction fractions were analyzed by inductively coupled plasma mass spectroscopy (ICP-MS) with a Perkin-Elmer Sciex ELAN 6000 apparatus and major elements (Al, Ca, Fe, K, Mg, Na, S, Cu and P) by inductively coupled plasma optical emission spectroscopy (ICP-OES) using a Thermo Fischer ICAP 6000 series (6500 Radial) spectrometer. The analytical uncertainties of the ICP measurements were ± 5% for both ICP-OES and ICP-MS. Using the standard reference material SRM 1633b (National Institute of Standards and Technology (NIST)) for trace elements in coal fly ash and ICP multi-element standard solutions (Merck), internal standards were intercalated between samples to check the analytical accuracy. The deviation from the stipulated values was always lower than 5%.

Concentrations of the major elements (Al, Fe, P, K, Ca, Mg, Na, S and Si) of the estuarine water samples were determined by Inductively Coupled Plasma-Atomic Emission Spectroscopy (ICP-AES; Jobin Yvon Ultima 2). Concentrations of the trace elements (Li, Be, B, Sc, Ti, V, Cr, Mn, Co, Ni, Cu, Zn, Ga, Ge, As, Se, Rb, Sr, Y, Zr, Nb, Mo, Cd, Sn, Sb, Cs, Ba, La, Ce, Pr, Nd, Sm, Eu, Gd, Tb, Dy, Ho, Er, Tm, Yb, Lu, Hf, Ta, W, Pb, Bi, Th and U) of these samples were determined by Inductively Coupled Plasma-Mass Spectrometry (ICP-MS) with a Thermo Scientific iCAP TQ ICP-MS without any prior dilution using Kinetic energy Discrimination - Argon Gas Dilution (KED-AGD mode). For trace element determinations, an internal solution containing Be, Sc, Ge, Rh and Ir was added on-line to the samples to correct signal drifts. Estuarine water and seawater certified reference materials for trace metals (SLEW-3 and CASS-6) were also analyzed to check the analytical accuracy. Detection limits were between 0.02 mg L^{-1} and 0.2 mg L^{-1} for major elements and ranged between 0.23 μg L^{-1} (Zn) and 3.44 pg L^{-1} (La) for trace elements. A detailed information of the REE measurement of the estuarine samples of this study using ICP-MS is provided in the supplementary information.

2.5. Water mixing and adsorption model

A water-mixing model was formulated using two end-member waters: the most AMD-influenced water (RTI-A sampling point with pH = 2.98) and the most seawater-influenced one (RTI-3 sampling point with a pH = 7.86). Calculations using the aqueous concentrations of trace and major elements measured by ICP-MS and ICP-OES were made using the PHREEQC code (Parkhurst and Appelo, 1999). Speciation of the elements was calculated using the Donee Thermoddem_V1.10 (Blanc et al., 2012) database, which was updated with the stability constants at standard conditions for the inorganic complexes of lanthanides and yttrium (Lee and Byrne, 1992; Millero, 1992; Klungness and Byrne, 2000; Luo and Byrne, 2001, 2004; Schijf and Byrne, 2004; Luo and

Millero, 2004). The solubility products of lanthanides and yttrium solid phases were imported from the LLNL database (Johnson et al., 2000) and other authors (Spahiu and Bruno, 1995). The chloride ion (Cl^-) was selected to balance solution charges. The mixing model used different percentages of the RTI-A and RTI-3 solutions to define intermediate solutions in order to emulate the estuarine mixing process without involving mineral precipitation or elemental sorption. Saturation indexes (*SI*) were calculated using the analytical data from the supernatant water of the cores. When $SI > 0$ the solid phase is saturated and therefore tends to precipitate, when $SI = 0$ the solid phase is in equilibrium with the water solution, and when $SI < 0$ the solid phase is undersaturated and therefore is dissolving.

After the mixing calculation, a REE adsorption model was implemented by taking into consideration the reactive surfaces of the main Al- and Fe-precipitates in AMD neutralization (i.e., schwertmannite and basaluminite). For schwertmannite, 4.75 sites nm^{-2} and a specific surface area of 200 $m^2\ g^{-1}$ were selected (Regenspurg et al., 2004; Antelo et al., 2012; Lozano et al., 2020a; Schoepfer and Burton, 2021). For basaluminite, the specific surface area was 68 $m^2\ g^{-1}$ and the number of surface sites was 4.6 sites nm^{-2} (Carrero et al., 2017a; Lozano et al., 2019a). The solid:liquid ratio was allowed to vary to check the conditions in which the model reproduced the field results. The REE adsorption data was taken from Lozano et al. (2019a, 2020a) and from Gutiérrez-León et al. (2023). The adsorption reactions (monodentate and bidentate surface complexes with schwertmannite and monodentate surface complexes with basaluminite) are expressed as:

$$LnSO_4^+ + nXOH \leftrightharpoons (XO)_nLnSO_4^{1-n} + nH^+, logK_{Ln} \quad (1)$$

where K_{Ln} is the equilibrium constant of the reaction, *XOH* is a free site of the mineral, $LnSO_4^+$ represents the aqueous REE-sulphate species and $(XO)_nLnSO_4^{1-n}$ is an occupied site. The stochiometric coefficient *n* in Eq. (1) can be 1 or 2 depending on the free site (*XOH*) used in the adsorption of $LnSO_4^+$, resulting in monodentate ($(XO)LnSO_4^0$) or bidentate ($(XO)_2LnSO_4^-$) surface complexes, respectively. The $logK_{Ln}$ values for the adsorption reactions are listed in Table S2 in the supplementary information (SI). The model is as a non-electrostatic surface complexation model (NEM-SC) as it does not consider the electrostatic forces involved in the adsorption of the $LnSO_4^+$ aqueous complex.

3. Results and discussion

3.1. Water chemistry and speciation of REE

Tables 1 and S2 list the concentrations of relevant major and trace elements analyzed at the different sampling points. The concentrations of REEs and yttrium decrease towards the more seawater-influenced samples owing to an increase in pH, which triggers sorption and precipitation reactions, and a dilution process (Lecomte et al., 2017). This depletion is clearly observed in the NASC-normalized REE patterns shown in Fig. 4, where the concentrations differ by several orders of magnitude from the AMD inlet (RTI-A and RTI-B sampling points) to the less AMD-influenced samples (RTI-3 sampling point). Concentrations of REEs obtained from our study and from previous experimental data provided by Lecomte et al. (2017) are of the same order of magnitude at their respective pH. The $(La/Yb)_{NASC}$ ratios (Table 1) present values that range between 0.45 and 0.85, with the lowest value at the most acidic pH. An abnormal value ($(La/Yb)_{NASC} = 3.93$) is obtained near the phosphogypsum stack (RTI-2 sample; Fig. 2). Except for the last point, there is a predominance of HREEs over LREEs in the estuarine water (Fig. 4). The $(La/Gd)_{NASC}$ ratio ranges between 0.26 and 0.82 and shows the same increasing tendency with increasing pH, without any anomaly at RTI-2. This means that at the RTI-2 sampling point, phosphogypsum leaches more LREEs and MREEs than HREEs. This coincides with the heterogeneous REE distribution described for byproducts of this type of material (Borrego et al., 2004). The Eu/Eu* ratio (i.e., Eu_{NASC} /(Sm_{NASC}

Table 1
pH, concentrations of REEs (μg L^{-1}) and $(La/Yb)_{NASC}$, $(La/Gd)_{NASC}$, Eu/Eu* and Ce/Ce* ratios of the supernatant water samples collected at each sampling point, except for RTI-A (shallow water suspension).

sample	pH	Y	La	Ce	Pr	Nd	Sm	Eu	Gd	Tb	Dy	Ho	Er	Tm	Yb	Lu	$(La/Yb)_{NASC}$	$(La/Gd)_{NASC}$	Eu/Eu*	Ce/Ce*
RTI-A	3.02	35.70	12.79	38.02	5.14	23.64	6.44	1.40	8.10	1.23	6.85	1.30	3.61	0.46	2.83	0.43	0.45	0.26	0.87	1.10
RTI-B	2.98	35.89	13.23	37.88	5.16	24.15	6.60	1.48	8.14	1.24	6.69	1.28	3.42	0.45	2.73	0.42	0.48	0.27	0.91	1.07
RTI-C	3.33	23.95	8.88	24.59	3.34	15.28	4.30	0.93	5.11	0.78	4.21	0.82	2.23	0.30	1.75	0.27	0.51	0.29	0.89	1.05
RTI-D	3.35	18.19	7.22	19.97	2.57	12.39	3.34	0.66	3.99	0.59	3.36	0.64	1.71	0.24	1.36	0.20	0.53	0.30	0.81	1.08
RTI-E	3.69	14.98	5.52	15.32	2.05	9.18	2.52	0.60	3.15	0.46	2.51	0.48	1.33	0.18	1.03	0.14	0.54	0.29	0.95	1.06
RTI-0	5.20	10.54	4.08	10.67	1.32	5.77	1.45	0.30	2.03	0.29	1.58	0.33	0.89	0.12	0.66	0.10	0.62	0.34	0.78	1.07
RTI-1	5.40	4.40	1.91	4.38	0.54	2.56	0.65	0.14	0.78	0.11	0.57	0.12	0.35	0.03	0.23	0.05	0.85	0.41	0.89	1.01
RTI-2	6.48	0.42	0.33	0.42	0.05	0.14	0.04	0.01	0.07	<DL	0.03	0.005	0.01	<DL	0.008	<DL	3.93	0.82	1.08	0.79
RTI-3	7.66	0.14	0.01	0.03	<DL	<DL	<DL	<DL	<DL	<DL	<DL	<DL	<DL	<DL	<DL	<DL	–	–	–	–

DL = detection limit.

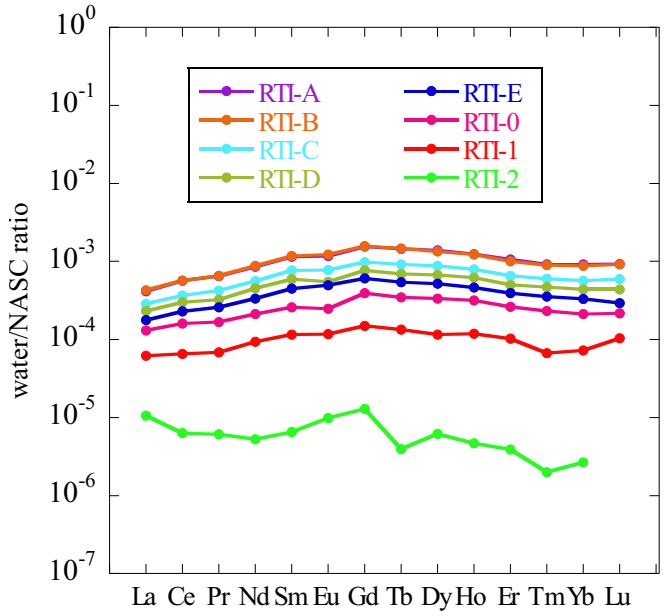

Fig. 4. NASC-normalized REE patterns of the water samples collected in the estuary.

$+ Gd_{NASC})^{0.5}$) shows a very slight negative anomaly (values from 0.78 to 0.95) at all sampling points except the RTI-2 sampling point, which presents a very slight positive anomaly (1.08). By contrast, the Ce/Ce* ratio (i.e., $Ce_N/(La_N + Pr_N)^{0.5}$) shows slightly positive anomalies (values between 1.01 and 1.12) in all samples except for RTI-2, which displays a very slight negative anomaly (0.79). Although RTI-0 is also close to the phosphogypsum stack, this pattern is only observed at RTI-2 sample.

Speciation of REEs under estuarine conditions is dependent on pH and REE (Fig. 5). For the speciation of the REE carbonate complexes, water samples were in equilibrium with respect to atmospheric CO_2. In LREE (Fig. 5b), the predominant complex is $LnSO_4^+$ (Ln = lanthanide), followed by Ln^{3+}. However, from RTI-2 to RTI-3, the $LnSO_4^+$ and Ln^{3+} molar fractions drop and carbonate complexes ($LnCO_3^+$) start to be relevant. As regards HREEs (Fig. 5a), the $LnSO_4^+$ molar fraction is significantly lower (20% less) whereas Ln^{3+} presents a higher molar fraction. As pH increases, the fractions of these aqueous complexes diminish in contrast to the increase in carbonate and hydroxide complexes. Chloride complexes ($LnCl^{2+}$) present molar fractions between 4% and 18% (LREE to HREE, respectively). Note, however, that as Cl^- is used for the charge balance, this value may change slightly. It is significant to REE speciation that the aqueous sulphate complexes adsorb onto schwertmannite and basaluminite (Lozano et al., 2019a, 2019b,c) as other complexes (e.g. Ln^{3+}) are much less reactive. However, free ion species are reactive with other ferric oxides (Marmier et al., 1997; Rabung et al., 1998; Marmier and Fromage, 1999; Liu et al., 2017).

3.2. Solid characterization and stability of Fe- and Al- precipitates

XRD analyses of the solid samples confirmed the presence of amorphous phases in the colloidal and sediment materials (Fig. S1). The most highly ordered Fe-bearing phases were jarosite and hematite. Goethite was not present. Quartz, illite, chlinochlore and kaolinite were identified. Silicates were considered to be erosion products from the host rock with no influence on the geochemistry of the estuarine waters aside from adsorption or exchange of some elements, including REEs (Wu et al., 2023).

As for the stability of the crystalline oxides, oxyhydroxysulphates and REE-phosphates, the *SI* for each solution are calculated and displayed as a function of pH (Fig. 6). Saturation indexes for K- and Pb-jarosites indicate that the minerals are saturated ($SI > 0$), Na- and H-jarosites are at equilibrium ($SI \approx 0$) or even undersaturated ($SI < 0$) (Fig. 6a), K- and Pb-jarosite are also undersaturated ($SI < 0$) at pH > 6. Thus, these precipitates will tend to form preferentially in the acidic parts of the estuary. The other relevant crystalline iron oxides (goethite and hematite) are saturated throughout the estuarine environment (Fig. 6b).

As regards the colloidal material, although hematite is the only crystalline metal-bearing oxyhydroxide, the elevated background in the XRD patterns (Fig. S1) indicates the existence of amorphous phases (Fig. 6c). The model, however, suggests the presence of schwertmannite and basaluminite at pH > 3.3 and 4.5, respectively, but at pH > 6.5, basaluminite is undersaturated ($SI < 0$), which could result in basaluminite re-dissolution with the consequent remobilization of adsorbed As, Se and REEs (Carrero et al., 2017b; Lozano et al., 2019a). On the other hand, ferrihydrite shows a constant positive *SI* index under all

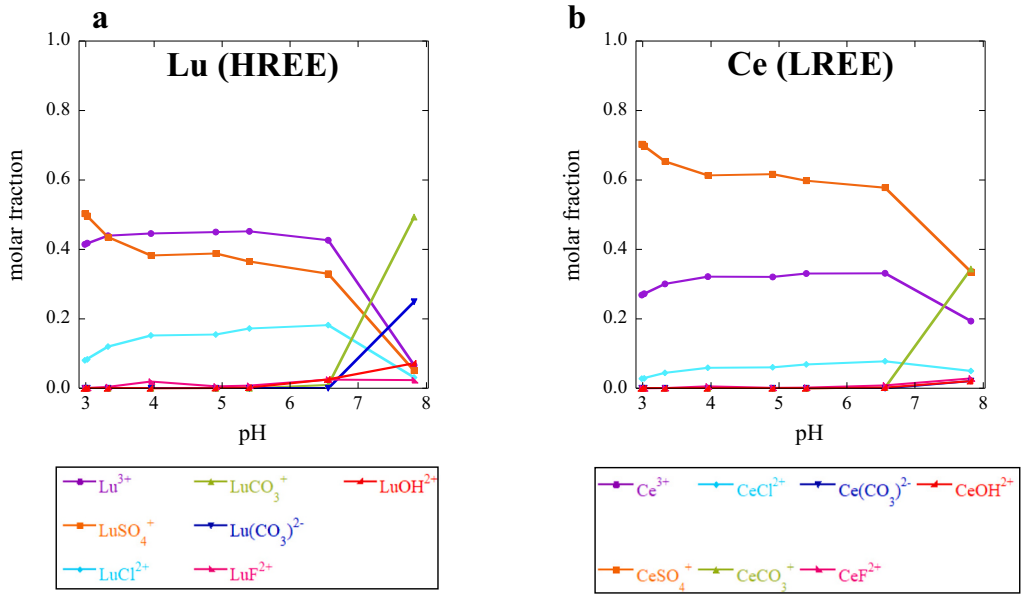

Fig. 5. Aqueous speciation of the collected water samples calculated as a function of pH with PHREEQC: (a) Lu (representative of HREEs) and (b) Ce (representative of LREEs).

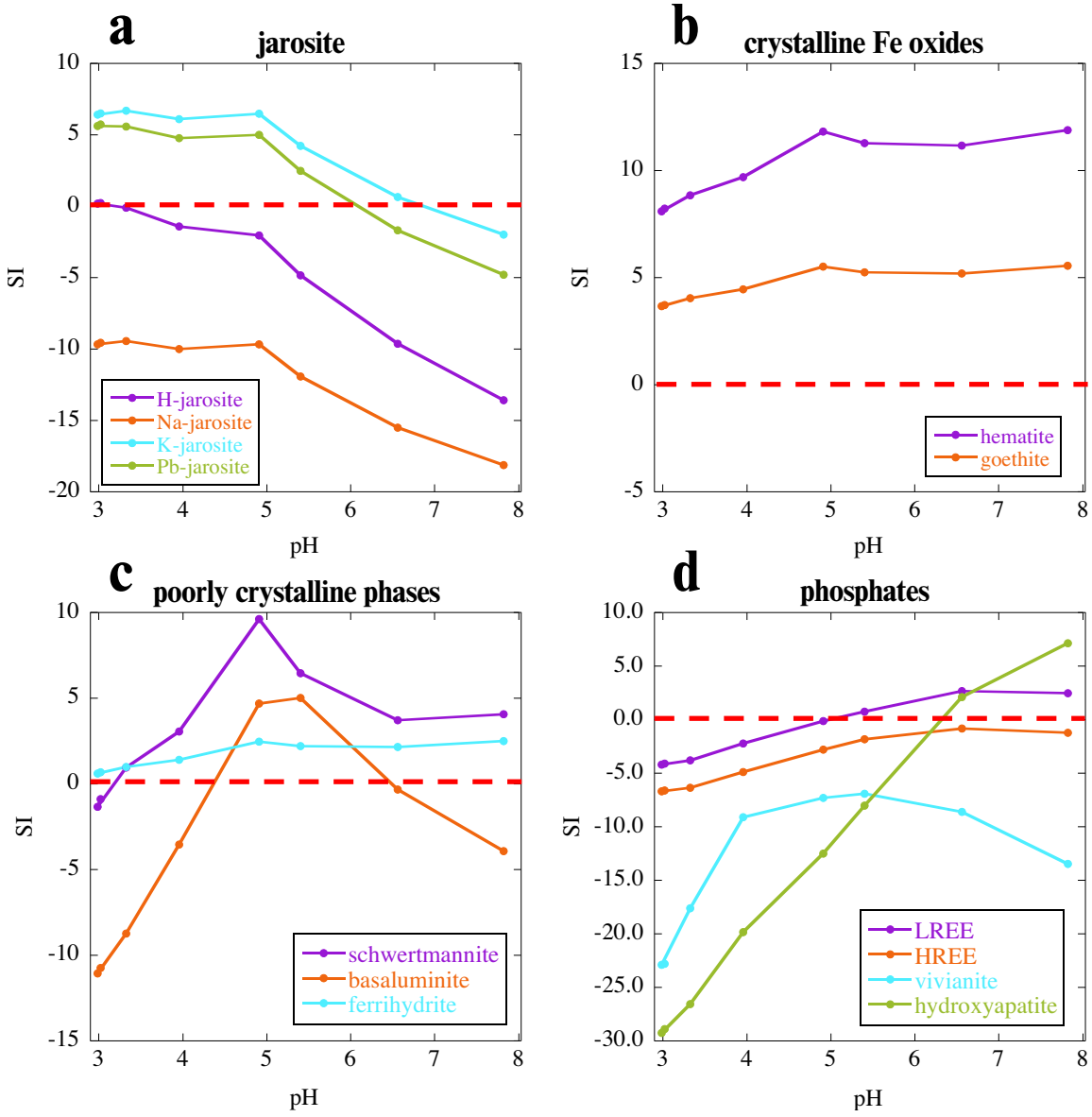

Fig. 6. Saturation indexes (SI) of the different phases that may be involved in the estuarine geochemistry, as function of pH, calculated with PHREEQC using the water chemistry measured in the estuary. The studied phases are (a) jarosites, (b) hematite and goethite, (c) schwertmannite, basaluminite and ferrihydrite, and (d) REE-phosphates and vivianite.

estuarine conditions. Phosphates present different behaviours (Fig. 6d); LREE-phosphates show a positive SI at pH > 5 whereas HREE-phosphates only show negative *SI* values, and MREEs present an intermediate behaviour (positive *SI* as LREE-phosphates tend to precipitate). Our geochemical models suggest that LREEs and MREEs are stable in some of the estuarine conditions whereas HREEs are not. However, other phosphates present in the phosphogypsum leachates (e.g., hydroxyapatite and strengite) are saturated at pH 5.5–7 (Papaslioti et al., 2018).

3.3. Mixing and adsorption models

The match for the concentrations calculated with the mixing model and those measured in field samples is shown in Fig. S2. As *SI* values with respect to Na-bearing phases (e.g. Na-jarosite) are negative, Na was considered to be a reference element, indicating when seawater mixing may affect the water chemistry of the estuary. In the model, the pH range for schwertmannite precipitation (i.e. pH between 3.3 and 3.5) was reached with a solution that contains a volume of 50% of each end-member. In contrast, to attain a pH of 6.2, the mixing solution needs to contain a volume of 95% of seawater and 5% of AMD, i.e., AMD waters need dilution.

Concentrations of alkaline and alkaline earth metals (K, Rb, Ca, Mg, Sr) in the mixing model satisfactorily match the field data (Fig. S2a). In contrast, Li and Ba concentrations are mostly overestimated and underestimated, respectively. This suggests that, except for Ba and Li, most alkaline and alkaline earth elements behave conservatively. Estuarine Ba concentrations might be tied to sulphate concentration as a depletion of sulphate, which is caused by newly formed Fe- and Al-oxyhydroxysulphates, could result in a Ba increase (Golding et al., 2018). However, an alternative source of Ba cannot be ruled out based on our mixing model.

For Co, Cu, Cd, Ni, Zn, Mn and Tl concentrations, the model and the field data show a good match (Fig. S2b), although the measured concentrations show different trends at Na concentrations above and below 7000 mg L^{-1} (pH 3.7–5.2), probably defining the onset of schwertmannite and basaluminite precipitations at the higher pH values. Thus, although sorption of divalent cations on estuarine Fe- and Al-phases

occur (Swedlund and Webster, 2001; Acero et al., 2006; Jönsson et al., 2006; Antelo et al., 2013; Fitzpatrick et al., 2017; Zhang et al., 2018), the aqueous concentration of these cations is mainly controlled by seawater mixing and, with the exception of Cu, they become quasi-conservative (Pérez-López et al., 2023). Moreover, the good match between field and model data suggests that the reactivity of these metals follows a trend (Cd < Ni < Tl < Zn < Mn < Co < Cu; Fig. S2b).

As for trivalent elements (Fig. S2c), Fe(III) is mostly depleted due to precipitation of Fe-bearing phases (e.g., schwertmannite, jarosite, goethite, hematite and ferrihydrite). Similarly, Al might co-precipitate with schwertmannite at pH ≈ 3.5–4 (Carrero et al., 2022) and precipitate as basaluminite at pH ≥ 4.5. Metals with different oxidation states (Pb and Cr) show different behaviours (Fig. S2c). Dissolution of Pb-Jarosite (Fig. 6a) might have a control over Pb concentration in the water at [Na] < 7000 mg L^{-1}, and the precipitation of schwertmannite and basaluminite might have an impact on the Pb concentration at [Na] > 7000 mg L^{-1}. Otherwise, Cr and Fe concentrations in the water show a similar tendency, suggesting a Cr sorption on Fe-bearing phases (e.g. schwertmannite) (Regenspurg and Peiffer, 2005; Antelo et al., 2012; Wang et al., 2021; Fan et al., 2023).

Concentrations of B and As (metalloids) present different behaviours (Fig. S2d). The model and the field concentrations of boron display a good match, i.e., [B] is controlled by seawater mixing (conservative element). In contrast, arsenic is depleted, which is probably due to arsenate incorporation onto Fe- and Al-bearing precipitates (Regenspurg and Peiffer, 2005; Loring et al., 2009; Antelo et al., 2012; Carrero et al., 2017b; Wang et al., 2021). The As distribution is discussed in the following section.

As for non-metals S and P (Fig. S2e), the model concentration of sulphur is slightly overestimated because of the precipitation of sulphate-bearing minerals (e.g., schwertmannite and basaluminite). The phosphorus concentration is extremely high at RTI-2 (near the phosphogypsum stack) compared to normal seawater probably due to phosphopgypsum leachates (Millán-Becerro et al., 2023). It is worth mentioning that the water is undersaturated with respect to hydroxyapatite at RTI-0 and RTI-1 (Figs. 2 and 3), and is saturated at RTI-2 and RTI-3, resulting in hydroxyapatite precipitation. This phase could be retaining some of the REEs (Owens et al., 2019).

Uranium is the only analyzed actinide presenting depletion when compared with the model data (Fig. S2f). It is known that dissolved and particulate uranium are controlled by adsorption–desorption processes and formation of carbonate complexes, both depending on pH (Hierro et al., 2013). At low pH, U tends to be dissolved and barely adsorbed by suspended particles. As pH increases, the adsorption onto Fe- and Al-particles occurs up to pH = 5.5, which is the pH of the minimum solubility. At pH > 5.5, dissolved uranium increases by carbonate complexation (Walter et al., 2003; Hierro et al., 2013; Mehta et al., 2015; Santofimia et al., 2022).

Field concentrations of REEs are lower than those of the mixing model (Fig. S2g). As [Na] < 7000 mg L^{-1}, the concentrations are slightly lower and influenced by seawater mixing. For [Na] > 7000 mg L^{-1}, however, the field concentrations are much lower. This change occurs at pH 3.7 (RTI-E) and pH 5.2 (RTI-0). In the pH range of 3.5–5.5, REEs adsorb onto precipitates of schwertmannite and basaluminite, making evident the buffer effect of the precipitating phases. The modeling of the REE adsorption shows two tendencies (Fig. 7), which may be accounted for by different solid:liquid ratios (S/L). With lower S/L ratios (e.g., S/L = 14 g L^{-1}), $SI_{schwertmannite} < 0$ and $SI_{basaluminite} < 0$ whereas for S/L = 50 g L^{-1} $SI_{schwertmannite} > 0$ and $SI_{basaluminite} > 0$. This indicates that precipitation of schwertmannite and basaluminite play a major role in REE

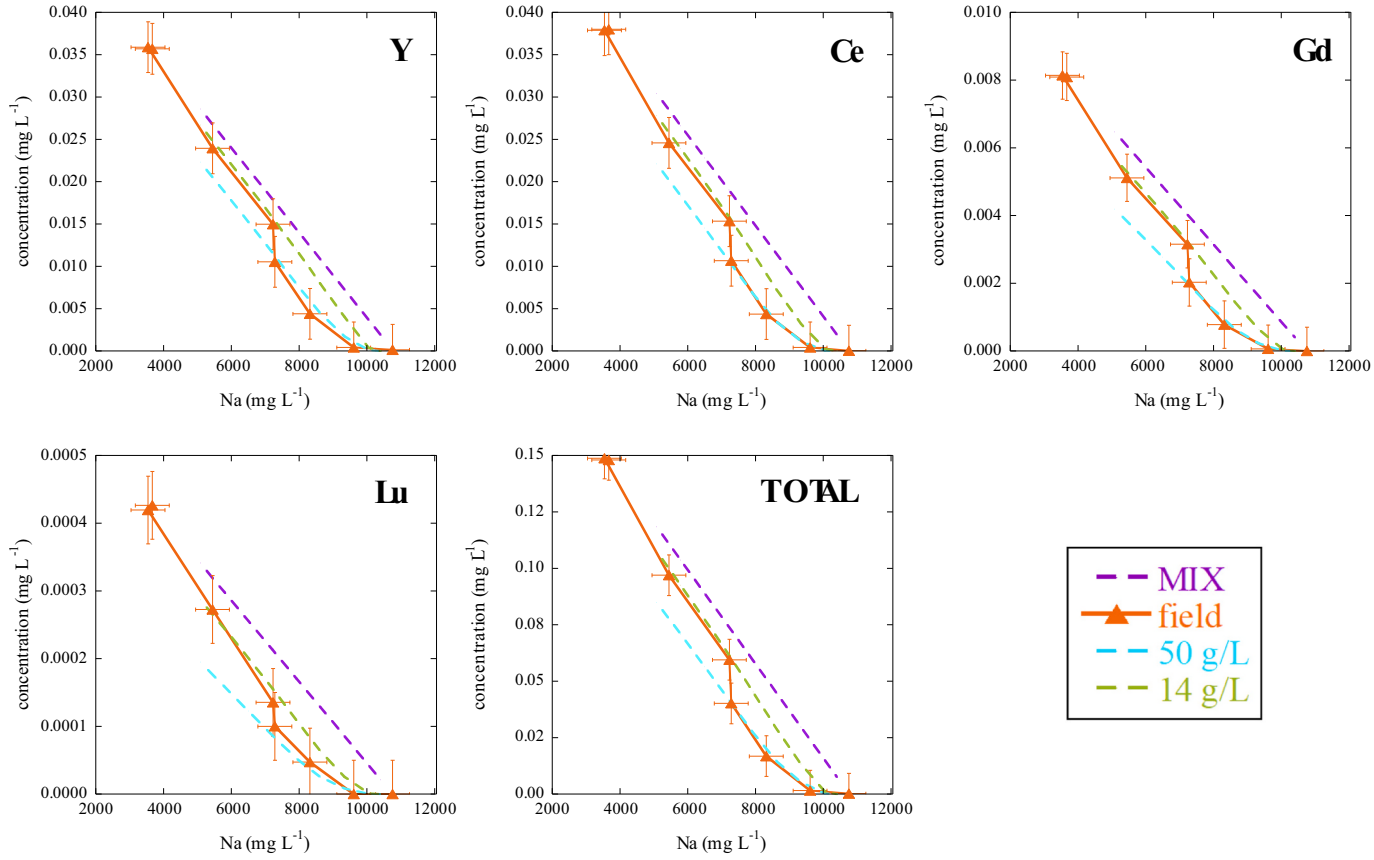

Fig. 7. Concentration of Y, Ce, Gd, Lu and total REE as function of Na concentration. Purple dashed lines correspond to the mixing model, green and blue dashed lines correspond to the adsorption model with a solid/liquid ratio of 14 g L^{-1} and 50 g L^{-1}, respectively. (For interpretation of the references to colour in this figure legend, the reader is referred to the web version of this article.)

scavenging, even though pH is not totally optimal for REE adsorption onto these minerals (Lozano et al., 2019a, 2020a). The elevated S/L is much higher than that obtained by filtration of the suspended material (≈ 0.5 g L^{-1}), suggesting a reactive estuarine sediment. Moreover, if the model results do apply to the whole estuary, schwertmannite and basaluminite should be present in areas where it is not saturated, which is only possible if sediment remobilization via tidal dynamics takes place.

3.4. Element distribution in the sediment

The element distribution in the sediment was studied using the results from the sequential extractions. Note that water-soluble phases contained in the sediments released most of the elements from the salts formed during sample lyophilization. These elements, therefore, are not part of the sediment, but were originally dissolved in water. Hence, the distribution of the elements can be discussed by only considering the other phases involved.

In the estuarine sediments, Ni and Mn are mainly present in the residual phase, with smaller amounts related to the highly and poorly ordered metal oxyhydroxides phases (Fig. S4a). It is known that the Ni adsorbed onto schwertmannite is released back to solution as schwertmannite transforms (ages) to goethite (Acero et al., 2006). Mn is released from dissolution of precipitated manganite (γ-MnOOH) in amonium oxalate at 80 °C, suggesting the presence of this phase in the poorly crystalline metal oxyhydroxide phases (Lee et al., 2002). Cd is mainly released by otavite ($CdCO_3$) and exchange phases. The presence of Cd in the carbonates depends on pH such that the highest the pH the highest the Cd concentration. Undersaturation with respect to otavite and calcite ($CaCO_3$) (Fig. S3) leads to Cd adsorption onto schwertmannite (Acero et al., 2006).

Zn, Cu and Co are the most reactive divalent elements with a high concentration in the exchange and both metal oxyhydroxide phases. Their concentrations in the sediment are distributed between the carbonate and exchange phase, and the poorly and highly ordered metal oxyhydroxide phases. Under extreme drought conditions, the divalent cations are scavenged by schwertmannite formed in acidic, sulphate soils (Fitzpatrick et al., 2017). With the exception of Mn, however, Co, Zn and Cd adsorbed onto schwertmannite at high pH are totally or partially released back to solution as schwertmannite ages to goethite (Acero et al., 2006; Kumpulainen et al., 2008). During schwertmannite ageing only 20% of total Cu is released back to solution, suggesting its presence in the highly ordered metal oxyhydroxides phases (Acero et al., 2006). Moreover, basaluminite can also retain some Cu and Ni at $5 \leq$ pH ≥ 7 conditions (Lu et al., 2021; Acero and Hudson-Edwards, 2022). Nonetheless, the scavenging of these elements by solid phases is not enough for a considerable alteration of the estuarine aqueous chemistry, apart from Cu (Fig. S2b). Trivalent Tl is closely related to highly ordered metal oxyhydroxide phases and its concentration in the sediments lowers with the influence of seawater (Fig. S4a).

Fe concentration in the sediment diminishes as pH increases, similarly to aqueous Fe in the estuarine waters (from 90 wt% to 30 wt% in AMD to seawater, respectively). Note that Fe in the poorly crystalized Fe-bearing phases that make up the sediments is Fe(III) (Lecomte et al., 2017) since aqueous Fe under the conditions of the estuarine system (oxic waters with a pH range of ≈ 3.5–8; Table S1) is Fe(III). At pH < 6.5, Fe is found in highly ordered metal oxyhydroxide phases (jarosite and goethite) whereas at pH ≥ 6.5 is present in amorphous metal oxyhydroxide phases (Fig. S4b). Cr is mainly present in the residual phase though an important amount is related to the poorly ordered metal oxyhydroxides. Although chromate can be preferentially sorbed onto schwertmannite at acidic pH (Regenspurg and Peiffer, 2005; Antelo et al., 2012; Wang et al., 2021), aqueous Cr in the liquid samples is rather scarce (< 10 μg L^{-1}). Al is mostly released by the poorly ordered metal oxyhydroxide phases but is also present in the residual phase and highly ordered metal oxyhydroxide phases. Al usually precipitates as basaluminite, which is a relevant sink for REEs and oxyanions (Carrero et al., 2017b; Lozano et al., 2019a), or may be incorporated in the structure of schwertmannite (Sánchez-España et al., 2016; Carrero et al., 2017b, 2022).

Pb is concentrated in the highly ordered metal oxyhydroxide phases (Fig. S4c). Its concentration remains constant in the pH range of 3.5–6.5 and decreases at pH of 7.5 (RTI-3 sampling point). As $SI_{\text{Pb-Jarosite}} > 0$ in the pH range of 3–6 (Fig. 6), Pb accumulates in the sediment as Pb-jarosite precipitates. Pb-jarosite can precipitate in the presence of sulphate and chloride (Dutrizac and Dinardo, 1983), showing a high capacity to retain Zn and Cu via coprecipitation. Partial dissolution of Pb-jarosite is possible under both alkali and acidic conditions (Smith et al., 2006), which could be the cause of the decrease in Pb concentration in the sediment at the RTI-3 sampling point in which $SI_{\text{Pb-Jarosite}} < 0$. The presence of Pb, therefore, could become environmentally problematic if estuarine tidal dynamics or sediment remobilization affects Pb-jarosite under alkaline conditions. Note that the Pb concentration in the adsorbed phase is 250 mg kg^{-1}. Earlier studies show that most of Pb remains in the solid as schwertmannite ages (Acero et al., 2006) leading to a lead accumulation in the sediment.

As is mainly found in the highly ordered metal oxyhydroxide phase at pH < 6 (Fig. S4c). In contrast, at pH > 6 the As content is higher in the poorly ordered metal oxyhydroxide phases. At pH 7.5 (RTI-31 sampling point), however, the As concentration is low in the sediment but high in the water sample (Fig. S2d), suggesting that As desorbs from the oxyhydroxide minerals at high pH, in accordance with previous studies (Regenspurg and Peiffer, 2005; Burton et al., 2009; Antelo et al., 2012; Carrero et al., 2017b; Wang et al., 2021). Sorption of arsenate in highly and poorly ordered metal oxyhydroxide phases occurs mainly in goethite (Manning et al., 1998; Gimenez et al., 2007; Loring et al., 2009; Burton et al., 2009), schwertmannite (Regenspurg and Peiffer, 2005; Antelo et al., 2012; Wang et al., 2021), basaluminite (Carrero et al., 2017b) and jarosite (Savage et al., 2005; Smith et al., 2006; Asta et al., 2009).

Concentrations of P are about 2–3 wt% at all sampling points except at RTI-2 with a 10 wt% (Fig. S4d). At this point, P is mainly found in the poorly ordered metal oxyhydroxide phase and is associated with the phosphate precipitates (Caraballo et al., 2011a; Ayora et al., 2016; Lozano et al., 2020b) and schwertmannite (Fan et al., 2023). The high concentrations of phosphate can stabilize schwertmannite by the formation of strong surface complexes, preventing thus schwertmannite ageing (Schoepfer et al., 2017, 2019). Moreover, the increase in P occurs with an increase in Fe(III) in the poorly ordered metal oxyhydroxide phases (Fig. S4b), indicating that schwertmannite ageing is inhibited in the presence of high concentrations of phosphate.

U shows a high affinity for the carbonate-exchange and poorly ordered metal oxyhydroxide phases (Fig. S4d). U concentration in the sediment increases with pH and achieves a maximum at the RTI-2 sampling point, where U(IV) from the phosphogypsum stack is probably immobilized by phosphate and carbonate precipitates (Hierro et al., 2013; Mehta et al., 2015; Millán-Becerro et al., 2023) and schwertmannite (Walter et al., 2003; Nishimura et al., 2009; Santofimia et al., 2022). Hence, phosphate enhances schwertmannite stability and may notably influence the U chemistry in the estuarine sediment. However, the forming of its own U-phosphate phase is also likely to occur.

The REEs NASC normalized patterns display a pH dependence (Fig. 8). At acidic pH (Fig. 8a,b) the sediments are depleted in REEs with respect to NASC whereas under neutral acidic pH the patterns approach the normalized values. At acidic pH, the depleted normalized REE patterns in the sediments contrast with the enriched REE patterns (compared with pH-neutral conditions) of the water analyzed at the sampling points (Fig. 4). Although REEs mainly concentrate in the residual phase, other phases are relevant as pH increases. The $(La/Yb)_{NASC}$, $(La/Gd)_{NASC}$, Eu/Eu* and Ce/Ce* ratios for the relevant phases in the sequential extraction and for the bulk sediment are listed in Table 2. In the bulk sediment, the $(La/Yb)_{NASC}$ and the $(La/Gd)_{NASC}$

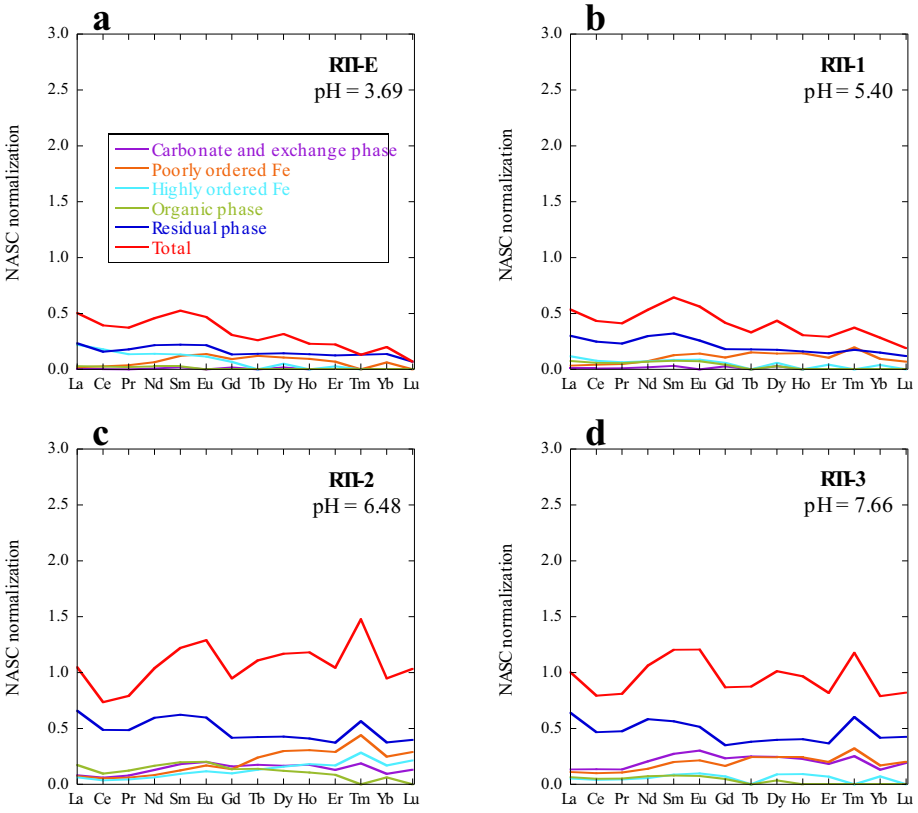

Fig. 8. NASC-normalized REE patterns of the sediment samples collected in the estuary: a) RTI-E, b) RTI-1; c) RTI-2 and d) RTI-3 (see Fig. 2).

Table 2
$(La/Yb)_{NASC}$, $(La/Gd)_{NASC}$, Eu/Eu* and Ce/Ce* ratios obtained from the sequential extractions of the sediment and colloidal matter samples collected at each sampling point.

	total				carbonate and exchange phases			
sample	$(La/Yb)_{NASC}$	$(La/Gd)_{NASC}$	Eu/Eu*	Ce/Ce*	$(La/Yb)_{NASC}$	$(La/Gd)_{NASC}$	Eu/Eu*	Ce/Ce*
RTI-E	2.52	1.63	1.16	0.91	–	0.15	–	–
RTI-0	1.89	1.28	1.09	0.92	–	0.30	–	0.93
RTI-2	1.11	1.11	1.20	0.81	0.86	0.50	1.17	0.75
RTI-3	1.27	1.15	1.18	0.88	1.02	0.58	1.20	1.02
colloids 4.5	1.06	0.91	1.10	0.97	0.56	0.36	1.20	1.04
colloids 5.5	1.30	1.13	1.18	0.98	0.51	0.34	1.26	1.00

	poorly ordered Fe-oxides				highly ordered Fe-oxides			
sample	$(La/Yb)_{NASC}$	$(La/Gd)_{NASC}$	Eu/Eu*	Ce/Ce*	$(La/Yb)_{NASC}$	$(La/Gd)_{NASC}$	Eu/Eu*	Ce/Ce*
RTI-E	0.31	0.21	1.30	1.00	–	3.27	1.21	1.04
RTI-0	0.36	0.32	1.21	1.02	3.03	2.03	1.25	0.89
RTI-2	0.30	0.54	1.30	0.82	0.37	0.64	1.23	0.71
RTI-3	0.65	0.67	1.18	0.93	0.74	0.73	1.24	0.84
colloids 4.5	0.58	0.45	1.29	1.09	1.61	1.08	1.40	0.95
colloids 5.5	0.45	0.40	1.29	1.21	1.56	1.08	1.33	0.98

	residual phase			
sample	$(La/Yb)_{NASC}$	$(La/Gd)_{NASC}$	Eu/Eu*	Ce/Ce*
RTI-E	1.68	1.74	1.21	0.78
RTI-0	2.00	1.65	1.25	0.94
RTI-2	1.75	1.58	1.23	0.86
RTI-3	1.53	1.82	1.24	0.85
colloids 4.5	1.66	2.16	1.40	0.91
colloids 5.5	2.07	2.14	1.33	0.95

ratios show an enrichment in LREEs with respect to HREEs and MREEs, respectively, which is pH dependent. The enrichment is higher at acidic pH (e.g., $(La/Yb)_{NASC} = 2.5$ and $(La/Gd)_{NASC} = 1.6$ in the RTI-E1 sample) than at circumneutral pH (e.g., $(La/Yb)_{NASC} = 1.27$ and $(La/Gd)_{NASC} = 1.15$ in the RTI-3 sample). Carbonate, exchange and poorly-ordered metal oxyhydroxide phases display low $(La/Yb)_{NASC}$ and $(La/Gd)_{NASC}$ ratios, suggesting an enrichment of MREES and HREEs with respect to LREEs in these phases. This is consistent with the sorption experiments of REE onto basaluminite and schwertmannite (Lozano et al., 2019a, 2020a), in which the sorbed fraction of HREEs and MREEs was higher than that of LREEs. By contrast, the $(La/Yb)_{NASC}$ and the $(La/Gd)_{NASC}$ ratios of the residual and highly ordered metal oxyhydroxide phases are high, especially at acidic pH, indicating and enrichment of LREEs in these phases. The Eu/Eu* ratio in the sediments presents a slightly positive anomaly (1.09–1.20) whereas the Ce/Ce* ratio does not present any relevant anomaly (values between 0.81 and 0.98). The slightly positive anomalies of the Eu/Eu* ratios in the sediment contrast with the slightly negative anomalies in the aqueous phase, suggesting a preference for Eu to accumulate in the sediment. However, the oxic conditions of the surface waters of the estuary do not facilitate the formation of aqueous Eu^{2+} (Sverjensky, 1984). Moreover, these anomalies could be related to the redox oscillations in the phosphogypsum waste (Papaslioti et al., 2020). But this hypothesis needs further investigation.

4. Conclusions

According to the field and model data of this study, three processes that affect the geochemistry of the estuary of Ría de Huelva are identified:

i) Mixing between AMD-river water and seawater is responsible for the behaviour of pH and conservative elements (Na, Ca, B, K, Rb, Mg and Sr). Some mining-related heavy metals (e.g., Cd, Ni, Zn and Mn) may also be considered conservative since they present a similar behaviour. However, large volumes of seawater are required to neutralize the acidity of the river water (in 1 L of AMD-seawater mixture, 95% must be seawater to attain a pH of 6.2).

ii) Precipitation of iron and aluminium oxy-hydroxysulphates (colloids) occurs as direct consequence of the increase in pH and the high concentrations of aqueous Fe and Al. These newly formed colloids, which consist of poorly ordered material, can retain other elements (i.e., Cu, Pb, Cr, As, P, REEs and smaller amounts of Zn, Co, Ni and Mn) via sorption and/or coprecipitation. As sorption is affected by pH, REEs are more abundant into these phases under high pH conditions. Other elements, such as As, are more plentiful in the sediment at acidic pH and their concentration is reduced as pH increases. Our REE model, which combines mixing and adsorption processes, is able to reproduce the behaviour of the aqueous REEs, requiring high S/L ratios at pH $\geq$ 3.5. At this pH, precipitation of schwertmannite occurs. The high S/L ratio in the model is necessary to match the field data and is only possible if also the sediment (in addition to the colloids) participates in the reactions. Below this pH some adsorption does occur but requiring a smaller S/L ratio. The smaller ratio could be brought about by sediment and/or colloid remobilization via tidal dynamics.

iii) The phosphogypsum stack from a nearby phosphate fertilizer plant has a notorious impact on the geochemistry of the surrounding estuarine environment. A characteristic feature of this process is that the release of high quantities of phosphate, which is shown in earlier works and observed in our sequential extractions, contributes to maintain the Fe stability in the poorly ordered oxyhydroxysulphate phases (schwertmannite). This in turn enhances the capacity of retaining other elements (U and REEs) released by the phosphogypsum or transported by the AMD-impacted river.

CRediT authorship contribution statement

Joan Gutiérrez-León: Writing – review & editing, Writing – original draft, Visualization, Methodology, Investigation, Conceptualization. **Ricardo Millán-Becerro:** Writing – review & editing, Methodology, Conceptualization. **Sergio Carrero:** Writing – review & editing, Methodology, Funding acquisition, Conceptualization. **Rafael Pérez-López:** Writing – review & editing, Methodology, Funding acquisition, Conceptualization. **Elina Ceballos:** Writing – review & editing, Methodology. **Rémi Freydier:** Writing – review & editing, Methodology. **Josep M. Soler:** Writing – review & editing, Supervision, Funding acquisition. **Jordi Cama:** Writing – review & editing, Supervision, Funding acquisition.

Declaration of competing interest

The authors declare that they have no known competing financial interests or personal relationships that could have appeared to influence the work reported in this paper.

Data availability

Data will be made available on request.

Acknowledgements

This work is part of the CGL2017-82331-R, PID2020-119196RB-C21 and PID2020-119196RB-C22 projects funded by MCIN/AEI/10.13039/501100011033/, with contribution of FEDER funds, and by the 2021SGR00308 project funded by the Catalan Government. IDAEA-CSIC is a Severo Ochoa Center of Research Excellence (Spanish Ministry of Science and Innovation, Project CEX2018-000794-S). We would like to acknowledge the technical assistance of N. Moreno, J. Bellés, R. Batrolí and M. Cabanas (IDAEA-CSIC) and Léa Causse (AETE-ISO platform, OSU OREME, University of Montpellier). We also thank the editor (Dr. Karen H. Johannesson) and two anonymous reviewers for their constructive comments that helped us to improve the quality of the manuscript.

Appendix A. Supplementary data

Supplementary data to this article can be found online at https://doi.org/10.1016/j.chemgeo.2024.122208.

References

Acero, P., Hudson-Edwards, K.A., 2022. Trace element uptake in fresh and aged aluminium oxyhydroxysulfates and hydroxides: Implications for mine drainage-affected environments. Appl. Geochem. 146, 105444.

Acero, P., Ayora, C., Torrentó, C., Nieto, J.M., 2006. The behavior of trace elements during schwertmannite precipitation and subsequent transformation into goethite and jarosite. Geochim. Cosmochim. Acta 70, 4130–4139.

Antelo, J., Fiol, S., Gondar, D., López, R., Arce, F., 2012. Comparison of arsenate, chromate and molybdate binding on schwertmannite: Surface adsorption vs anion-exchange. J. Colloid Interface Sci. 386, 338–343.

Antelo, J., Fiol, S., Gondar, D., Pérez, C., López, R., Arce, F., 2013. Cu(II) incorporation to schwertmannite: effect on stability and reactivity under AMD conditions. Geochim. Cosmochim. Acta 119, 149–163.

Asta, M.P., Cama, J., Martínez, M., Giménez, J., 2009. Arsenic removal by goethite and jarosite in acidic conditions and its environmental implications. J. Hazard. Mater. 171, 965–972.

Ayora, C., Caraballo, M.A., Macías, F., Rötting, T.S., Carrera, J., Nieto, J.M., 2013. Acid mine drainage in the Iberian Pyrite Belt: 2. Lessons learned from recent passive remediation experiences. Environ. Sci. Pollut. Res. 20, 7837–7853.

Ayora, C., Macías, F., Torres, E., Lozano, A., Carrero, S., Nieto, J.M., Pérez-López, R., Fernández-Martínez, A., Castillo-Michel, H., 2016. Recovery of rare Earth elements and Yttrium from Passive-Remediation Systems of Acid Mine Drainage. Environ. Sci. Technol. 50, 8255–8262.

Blanc, Ph., Lassin, A., Piantone, P., Azaroual, M., Jacquemet, N., Fabbri, A., Gaucher, E. C., 2012. Thermoddem: a geochemical database focused on low temperature water/rock interactions and waste materials. Appl. Geochem. 27, 2107–2116.
Borrego, J., López-González, N., Carro, B., Lozano-Soria, O., 2004. Origin of the anomalies in light and middle REE in sediments of an estuary affected by phosphogypsum wastes (South-Western Spain). Mar. Pollut. Bull. 49, 1045–1053.
Borrego, J., López-González, N., Carro, B., Lozano-Soria, O., 2005. Geochemistry of rare-earth elements in Holocene sediments of an acidic estuary: environmental markers (Tinto River Estuary, South-Western Spain). J. Geochem. Explor. 86, 119–129.
Borrego, J., Carro, B., López-González, N., de la Rosa, J., Grande, J.A., Gómez, T., de la Torre, M.L., 2012. Effect of acid mine drainage on dissolved rare earth elements geochemistry along a fluvial–estuarine system: the Tinto-Odiel Estuary (S.W. Spain). Hydrol. Res. 43, 262–274.
Braungardt, C.B., Achterberg, E.P., Elbaz-Poulichet, F., Morley, N.H., 2003. Metal geochemistry in a mine-polluted estuarine system in Spain. Appl. Geochem. 18, 1757–1771.
Burton, E.D., Bush, R.T., Johnston, S.G., Watling, K.M., Hocking, R.K., Sullivan, L.A., Parker, G.K., 2009. Sorption of arsenic (V) and arsenic (III) to schwertmannite. Environ. Sci. Technol. 43, 9202–9207.
Cánovas, C.R., Olías, M., Nieto, J.M., Sarmiento, A.M., Cerón, J.C., 2007. Hydrogeochemical characteristics of the Tinto and Odiel Rivers (SW Spain). Factors controlling metal contents. Sci. Total Environ. 373, 363–382.
Cánovas, C.R., Olías, M., Sarmiento, A.M., Nieto, J.M., Galván, L., 2012. Pollutant transport processes in the Odiel River (SW Spain) during rain events. Water Resour. Res. 48.
Cánovas, C.R., Macías, F., Pérez-López, R., 2016. Metal and acidity fluxes controlled by precipitation/dissolution cycles of sulfate salts in an anthropogenic mine aquifer. J. Contam. Hydrol. 188, 29–43.
Cánovas, C.R., Basallote, M.D., Macías, F., 2020. Distribution and availability of rare earth elements and trace elements in the estuarine waters of the Ría of Huelva (SW Spain). Environ. Pollut. 267, 115506.
Cánovas, C.R., Basallote, M.D., Macías, F., Freydier, R., Parviainen, A., Pérez-Lopez, R., 2022. Thallium distribution in an estuary affected by acid mine drainage (AMD): the Ría de Huelva estuary (SW Spain). Environ. Pollut. 306, 119448.
Caraballo, M.A., Rötting, T.S., Macías, F., Nieto, J.M., Ayora, C., 2009a. Field multi-step limestone and MgO passive system to treat acid mine drainage with high metal concentrations. Appl. Geochem. 24, 2301–2311.
Caraballo, M.A., Rotting, T.S., Nieto, J.M., Ayora, C., 2009b. Sequential extraction and DXRD applicability to poorly crystalline Fe- and Al-phase characterization from an acid mine water passive remediation system. Am. Mineral. 94, 1029–1038.
Caraballo, M.A., Macías, F., Nieto, J.M., Castillo, J., Quispe, D., Ayora, C., 2011a. Hydrochemical performance and mineralogical evolution of a dispersed alkaline substrate (DAS) remediating the highly polluted acid mine drainage in the full-scale passive treatment of Mina Esperanza (SW Spain). Am. Mineral. 96, 1270–1277.
Caraballo, M.A., Macías, F., Rötting, T.S., Nieto, J.M., Ayora, C., 2011b. Long term remediation of highly polluted acid mine drainage: a sustainable approach to restore the environmental quality of the Odiel river basin. Environ. Pollut. 159, 3613–3619.
Carrero, S., Fernandez-Martinez, A., Pérez-López, R., Lee, D., Aquilanti, G., Poulain, A., Lozano, A., Nieto, J.M., 2017a. The nanocrystalline structure of basaluminite, an aluminum hydroxide sulfate from acid mine drainage. Am. Mineral. 102, 2381–2389.
Carrero, S., Fernandez-Martinez, A., Pérez-López, R., Poulain, A., Salas-Colera, E., Nieto, J.M., 2017b. Arsenate and selenate Sscavenging by basaluminite: insights into the reactivity of aluminum phases in acid mine drainage. Environ. Sci. Technol. 51, 28–37.
Carrero, S., Fernandez-Martinez, A., Pérez-López, R., Cama, J., Dejoie, C., Nieto, J.M., 2022. Effects of aluminum incorporation on the schwertmannite structure and surface properties. Environ Sci Process Impacts 24, 1383–1391.
Chakhmouradian, A.R., Wall, F., 2012. Rare earth elements: minerals, mines, magnets (and more). Elements 8, 333–340.
Dold, B., 2003. Speciation of the most soluble phases in a sequential extraction procedure adapted for geochemical studies of copper sulfide mine waste. J. Geochem. Explor. 80, 55–68.
Dutrizac, J.E., Dinardo, O., 1983. The co-precipitation of copper and zinc with lead jarosite. Hydrometallurgy 11, 61–78.
Elbaz-Poulichet, F., Dupuy, C., 1999. Behaviour of rare earth elements at the freshwater–seawater interface of two acid mine rivers: the Tinto and Odiel (Andalucia, Spain). Appl. Geochem. 14, 1063–1072.
Elbaz-Poulichet, F., Morley, N.H., Beckers, J.M., Nomerange, P., 2001. Metal fluxes through the Strait of Gibraltar: the influence of the Tinto and Odiel rivers (SW Spain). Mar. Chem. 73, 193–213.
Fan, C., Guo, C., Chen, W., Tao, L., Yao, Q., Lu, G., Shen, Y., Dang, Z., 2023. Chromate and phosphate adsorption on schwertmannite: competition, mobilization and mechanisms. Coll. Surf. A Physicochem. Eng. Asp. 658, 130691.
Ferreira da Silva, E., Bobos, I., Xavier Matos, J., Patinha, C., Reis, A.P., Cardoso Fonseca, E., 2009. Mineralogy and geochemistry of trace metals and REE in volcanic massive sulfide host rocks, stream sediments, stream waters and acid mine drainage from the Lousal mine area (Iberian Pyrite Belt, Portugal). Appl. Geochem. 24, 383–401.
Fitzpatrick, R.W., Mosley, L.M., Raven, M.D., Shand, P., 2017. Schwertmannite formation and properties in acidic drain environments following exposure and oxidation of acid sulfate soils in irrigation areas during extreme drought. Geoderma 308, 235–251.
Galán, E., Gómez-Ariza, J.L., González, I., Fernández-Caliani, J.C., Morales, E., Giráldez, I., 2003. Heavy metal partitioning in river sediments severely polluted by acid mine drainage in the Iberian Pyrite Belt. Appl. Geochem. 18, 409–421.
Gimenez, J., Martinez, M., Depablo, J., Rovira, M., Duro, L., 2007. Arsenic sorption onto natural hematite, magnetite, and goethite. J. Hazard. Mater. 141, 575–580.
Golding, L.A., McKnight, K., Binet, M., Adams, M., Apte, S.C., 2018. Toxicity of dissolved and precipitated forms of barium to a freshwater alga (*Chlorella* sp. 12) and water flea (*Ceriodaphnia dubia*). Environ. Toxicol. Chem. 37, 1632–1642.
Grande, J.A., Borrego, J., Morales, J.A., 2000. A study of heavy metal pollution in the Tinto-Odiel estuary in southwestern Spain using factor analysis. Environ. Geol. 39, 1095–1101.
Grande, J.A., Borrego, J., Morales, J.A., de la Torre, M.L., 2003. A description of how metal pollution occurs in the Tinto–Odiel rias (Huelva-Spain) through the application of cluster analysis. Mar. Pollut. Bull. 46, 475–480.
Grande, J.A., de la Torre, M.L., Cerón, J.C., Beltrán, R., Gómez, T., 2010. Overall hydrochemical characterization of the Iberian Pyrite Belt. Main acid mine drainage-generating sources (Huelva, SW Spain). J. Hydrol. (Amst). 390, 123–130.
Grande, J.A., Santisteban, M., de la Torre, M.L., Dávila, J.M., Pérez-Ostalé, E., 2018. Map of impact by acid mine drainage in the river network of the Iberian Pyrite Belt (Sw Spain). Chemosphere 199, 269–277.
Gwenzi, W., Mangori, L., Danha, C., Chaukura, N., Dunjana, N., Sanganyado, E., 2018. Sources, behaviour, and environmental and human health risks of high-technology rare earth elements as emerging contaminants. Sci. Total Environ. 636, 299–313.
Hierro, A., Martín, J.E., Olías, M., García, C., Bolivar, J.P., 2013. Uranium behavior during a tidal cycle in an estuarine system affected by acid mine drainage (AMD). Chem. Geol. 342, 110–118.
Johnson, J., Anderson, G., Parkhurst, D., 2000. Database "thermo.com.V8R6.230" Rev. 1.11., Livermore, California.
Jönsson, J., Sjöberg, S., Lövgren, L., 2006. Adsorption of Cu(II) to schwertmannite and goethite in presence of dissolved organic matter. Water Res. 40, 969–974.
Klungness, G.D., Byrne, R.H., 2000. Comparative hydrolysis behavior of the rare earths and yttrium: the influence of temperature and ionic strength. Polyhedron 19, 99–107.
Kumpulainen, S., Räisänen, M.L., Von Der Kammer, F., Hofmann, T., 2008. Ageing of synthetic and natural schwertmannites at pH 2—8. Clay Miner. 43, 437–448.
Lecomte, K.L., Sarmiento, A.M., Borrego, J., Nieto, J.M., 2017. Rare earth elements mobility processes in an AMD-affected estuary: Huelva Estuary (SW Spain). Mar. Pollut. Bull. 121, 282–291.
Lee, G., Bigham, J.M., Faure, G., 2002. Removal of trace metals by coprecipitation with Fe, Al and Mn from natural waters contaminated with acid mine drainage in the Ducktown Mining District, Tennessee. Appl. Geochem. 17, 569–581.
Lee, J.H., Byrne, R.H., 1992. Examination of comparative rare earth element complexation behavior using linear free-energy relationships. Geochim. Cosmochim. Acta 56, 1127–1137.
León, R., Macías, F., Cánovas, R., Pérez-López, R., Ayora, C., Nieto, J.M., Olías, M., 2021. Mine waters as a secondary source of rare earth elements worldwide: the case of the Iberian Pyrite Belt. J. Geochem. Explor. 224, 106742.
León, R., Macías, F., Cánovas, C.R., Millán-Becerro, R., Pérez-López, R., Ayora, C., Nieto, J.M., 2023. Evidence of rare earth elements origin in acid mine drainage from the Iberian Pyrite Belt (SW Spain). Ore Geol. Rev. 154, 105336.
Liu, H., Pourret, O., Guo, H., Bonhoure, J., 2017. Rare earth elements sorption to iron oxyhydroxide: Model development and application to groundwater. Appl. Geochem. 87, 158–166.
Loring, J.S., Sandström, M.H., Norén, K., Persson, P., 2009. Rethinking arsenate coordination at the surface of goethite. Chem. – A Euro J. 15, 5063–5072.
Lozano, A., Ayora, C., Fernández-Martínez, A., 2019a. Sorption of rare earth elements onto basaluminite: the role of sulfate and pH. Geochim. Cosmochim. Acta 258, 50–62.
Lozano, A., Fernández-Martínez, A., Ayora, C., Di Tommaso, D., Poulain, A., Rovezzi, M., Marini, C., 2019b. Solid and Aqueous Speciation of Yttrium in Passive Remediation Systems of Acid Mine Drainage. Environ. Sci. Technol. 53, 11153–11161.
Lozano, A., Ayora, C., Fernández-Martínez, A., 2020a. Sorption of rare earth elements on schwertmannite and their mobility in acid mine drainage treatments. Appl. Geochem. 113, 104499.
Lozano, A., Ayora, C., Macías, F., León, R., Gimeno, M.J., Auqué, L., 2020b. Geochemical behavior of rare earth elements in acid drainages: Modeling achievements and limitations. J. Geochem. Explor. 216, 106577.
Lu, C., Yang, B., Cui, X., Wang, S., Qu, C., Zhang, W., Zhou, B., 2021. Characteristics and environmental response of white secondary mineral precipitate in the acid mine drainage from Jinduicheng Mine, Shaanxi, China. Bull. Environ. Contam. Toxicol. 107, 1012–1021.
Luo, Y., Millero, F.J., 2004. Effects of temperature and ionic strength on the stabilities of the first and second fluoride complexes of yttrium and the rare earth elements. Geochim. Cosmochim. Acta 68, 4301–4308.
Luo, Y.R., Byrne, R.H., 2001. Yttrium and rare earth element complexation by chloride ions at 25°C. J. Solut. Chem. 30, 837–845.
Luo, Y.R., Byrne, R.H., 2004. Carbonate complexation of yttrium and the rare earth elements in natural waters. Geochim. Cosmochim. Acta 68, 691–699.
Macías, F., Caraballo, M.A., Nieto, J.M., Rötting, T.S., Ayora, C., 2012. Natural pretreatment and passive remediation of highly polluted acid mine drainage. J. Environ. Manag. 104, 93–100.
Macías, F., Pérez-López, R., Caraballo, M.A., Cánovas, C.R., Nieto, J.M., 2017. Management strategies and valorization for waste sludge from active treatment of extremely metal-polluted acid mine drainage: a contribution for sustainable mining. J. Clean. Prod. 141, 1057–1066.
Manning, B.A., Fendorf, S.E., Goldberg, S., 1998. Surface structures and stability of Arsenic(III) on Goethite: spectroscopic evidence for Inner-sphere complexes. Environ. Sci. Technol. 32, 2383–2388.

Marmier, N., Fromage, F., 1999. Comparing Electrostatic and Nonelectrostatic Surface Complexation Modeling of the Sorption of Lanthanum on Hematite. J. Colloid Interface Sci. 212, 252–263.
Marmier, N., Dumonceau, J., Fromage, F., 1997. Surface complexation modeling of Yb (III) sorption and desorption on hematite and alumina. J. Contam. Hydrol. 26, 159–167.
Mehta, V.S., Maillot, F., Wang, Z., Catalano, J.G., Giammar, D.E., 2015. Transport of U (VI) through sediments amended with phosphate to induce in situ uranium immobilization. Water Res. 69, 307–317.
Millán-Becerro, R., Pérez-López, R., Cánovas, C.R., Macías, F., León, R., 2023. Phosphogypsum weathering and implications for pollutant discharge into an estuary. J. Hydrol. (Amst) 617, 128943.
Millero, F.J., 1992. Stability constants for the formation of rare earth-inorganic complexes as a function of ionic strength. Geochim. Cosmochim. Acta 56, 3123–3132.
Nieto, J.M., Sarmiento, A.M., Canovas, C.R., Olias, M., Ayora, C., 2013. Acid mine drainage in the Iberian Pyrite Belt: 1. Hydrochemical characteristics and pollutant load of the Tinto and Odiel rivers. Environ. Sci. Pollut. Res. 20, 7509–7519.
Nishimura, K., Miura, O., Ito, D., Tsunasima, Y., Wada, Y., 2009. Removal of radioactive heavy metal ions from solution by superconducting high-gradient magnetic separation with Schwertmannite and Zirconium-Ferrite Adsorbents. IEEE Transact. Appl. Supercond. 19, 2162–2164.
Olías, M., Cánovas, C.R., Nieto, J.M., Sarmiento, A.M., 2006. Evaluation of the dissolved contaminant load transported by the Tinto and Odiel rivers (South West Spain). Appl. Geochem. 21, 1733–1749.
Owens, C.L., Nash, G.R., Hadler, K., Fitzpatrick, R.S., Anderson, C.G., Wall, F., 2019. Apatite enrichment by rare earth elements: a review of the effects of surface properties. Adv. Colloid Interf. Sci. 265, 14–28.
Papaslioti, E.M., Pérez-López, R., Parviainen, A., Sarmiento, A.M., Nieto, J.M., Marchesi, C., Delgado-Huertas, A., Garrido, C.J., 2018. Effects of seawater mixing on the mobility of trace elements in acid phosphogypsum leachates. Mar. Pollut. Bull. 127, 695–703.
Papaslioti, E.M., Pérez-López, R., Parviainen, A., Phan, V.T.H., Marchesi, C., Fernandez-Martinez, A., Garrido, C.J., Nieto, J.M., Charlet, L., 2020. Effects of redox oscillations on the phosphogypsum waste in an estuarine salt-marsh system. Chemosphere 242, 125174.
Parkhurst, D.L., Appelo, C.A.J., 1999. User's Guide to PhreeqC (Version 2.18): A Computer Program for Speciation, and Inverse Geochemical Calculations. U.S. Department of Interior.
Pérez-López, R., Macías, F., Cánovas, C.R., Sarmiento, A.M., Pérez-Moreno, S.M., 2016. Pollutant flows from a phosphogypsum disposal area to an estuarine environment: an insight from geochemical signatures. Sci. Total Environ. 553, 42–51.
Pérez-López, R., Millán-Becerro, R., Basallote, M.D., Carrero, S., Parviainen, A., Freydier, R., Macías, F., Cánovas, C.R., 2023. Effects of estuarine water mixing on the mobility of trace elements in acid mine drainage leachates. Mar. Pollut. Bull. 187, 114491.
Quispe, D., Pérez-López, R., Silva, L.F.O., Nieto, J.M., 2012. Changes in mobility of hazardous elements during coal combustion in Santa Catarina power plant (Brazil). Fuel 94, 495–503.
Rabung, T., Geckeis, H., Kim, J.I., Beck, H.P., 1998. Sorption of Eu(III) on a Natural Hematite: Application of a Surface Complexation Model. J. Colloid Interface Sci. 208, 153–161.
Regenspurg, S., Peiffer, S., 2005. Arsenate and chromate incorporation in schwertmannite. Appl. Geochem. 20, 1226–1239.
Regenspurg, S., Brand, A., Peiffer, S., 2004. Formation and stability of schwertmannite in acidic mining lakes 1 1Associate editor: C. M. Eggleston. Geochim. Cosmochim. Acta 68, 1185–1197.
Rutherford, P.M., Dudas, M.J., Samek, R.A., 1994. Environmental impacts of phosphogypsum. Sci. Total Environ. 149, 1–38.
Sánchez España, J., López Pamo, E., Santofimia, E., Aduvire, O., Reyes, J., Barettino, D., 2005. Acid mine drainage in the Iberian Pyrite Belt (Odiel river watershed, Huelva, SW Spain): Geochemistry, mineralogy and environmental implications. Appl. Geochem. 20, 1320–1356.
Sánchez-España, J., Yusta, I., Burgos, W.D., 2016. Geochemistry of dissolved aluminum at low pH: Hydrobasaluminite formation and interaction with trace metals, silica and microbial cells under anoxic conditions. Chem. Geol. 441, 124–137.
Santofimia, E., González, F.J., Rincón-Tomás, B., López-Pamo, E., Marino, E., Reyes, J., Bellido, E., 2022. The mobility of thorium, uranium and rare earth elements from Mid Ordovician black shales to acid waters and its removal by goethite and schwertmannite. Chemosphere 307, 135907.
Savage, K.S., Bird, D.K., O'Day, P.A., 2005. Arsenic speciation in synthetic jarosite. Chem. Geol. 215, 473–498.
Schijf, J., Byrne, R.H., 2004. Determination of SO4β1 for yttrium and the rare earth elements at I = 0.66 m and t = 25°C—implications for YREE solution speciation in sulfate-rich waters. Geochim. Cosmochim. Acta 68, 2825–2837.
Schoepfer, V.A., Burton, E.D., 2021. Schwertmannite: a review of its occurrence, formation, structure, stability and interactions with oxyanions. Earth Sci. Rev. 221, 103811.
Schoepfer, V.A., Burton, E.D., Johnston, S.G., Kraal, P., 2017. Phosphate-imposed constraints on schwertmannite stability under reducing conditions. Environ. Sci. Technol. 51, 9739–9746.
Schoepfer, V.A., Burton, E.D., Johnston, S.G., 2019. Contrasting effects of phosphate on the rapid transformation of schwertmannite to Fe(III) (oxy)hydroxides at near-neutral pH. Geoderma 340, 115–123.
Smith, A.M.L., Dubbin, W.E., Wright, K., Hudson-Edwards, K.A., 2006. Dissolution of lead- and lead–arsenic-jarosites at pH 2 and 8 and 20 °C: Insights from batch experiments. Chem. Geol. 229, 344–361.
Spahiu, K., Bruno, J., 1995. A Selected Thermodynamic Database for REE to Be Used in HLNW Performance Assessment Exercises.
Sverjensky, D.A., 1984. Europium redox equilibria in aqueous solution. Earth Planet. Sci. Lett. 67, 70–78.
Swedlund, P.J., Webster, J.G., 2001. Cu and Zn ternary surface complex formation with SO4 on ferrihydrite and schwertmannite. Appl. Geochem. 16, 503–511.
Walter, M., Arnold, T., Reich, T., Bernhard, G., 2003. Sorption of uranium(VI) onto ferric oxides in sulfate-rich acid waters. Environ. Sci. Technol. 37, 2898–2904.
Wang, X., Ying, H., Zhao, W., Feng, X., Tan, W., Beyer, K.A., Huang, Q., Liu, F., Zhu, M., 2021. Molecular-Scale Understanding of Sulfate Exchange from Schwertmannite by Chromate Versus Arsenate. Environ. Sci. Technol. 55, 5857–5867.
Wu, Z., Chen, Y., Wang, Y., Xu, Y., Lin, Z., Liang, X., Cheng, H., 2023. Review of rare earth element (REE) adsorption on and desorption from clay minerals: Application to formation and mining of ion-adsorption REE deposits. Ore Geol. Rev. 157, 105446.
Zhang, Z., Bi, X., Li, X., Zhao, Q., Chen, H., 2018. Schwertmannite: occurrence, properties, synthesis and application in environmental remediation. RSC Adv. 8, 33583–33599.